Supplementary Information

Aluminium Substitution in Sb_2S_3 Nanorods Enhance the Stability of Microstructure and High-Rate Capability in Alloying Regime

Akshay Kumar Budumuru,[a,b,#] Lokeswararao Yelamnchi,[a,#] and Chandran Sudakar[a,b,*]

[a.] *Multifunctional Materials Laboratory, Department of Physics, Indian Institute of Technology Madras, Chennai 600036, India. Email: csudakar@iitm.ac.in; Telephone: +91-44-2257-4895*

[b.] *Center for Advanced Materials and Microscopy, Indian Institute of Technology Madras, Chennai 600036, India.*

\# These authors have contributed equally.

Table S1. The estimated atomic composition of the anodes from EDS along with the atomic ratio calculated from the precursors used in synthesis.

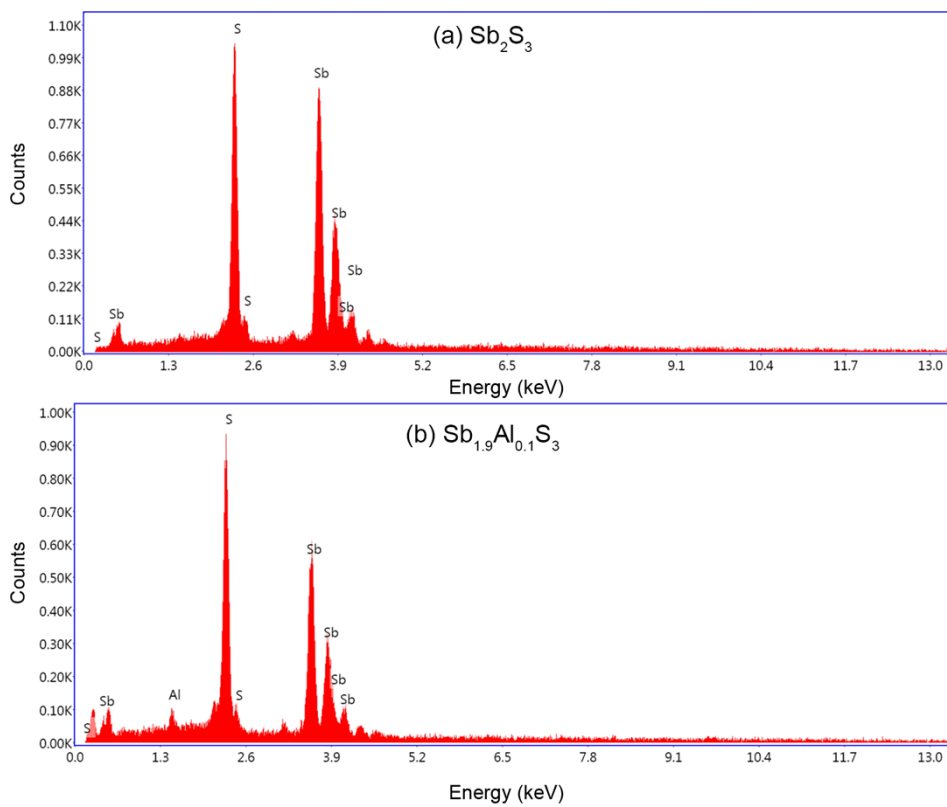| Sample ID	Chemical analysis	$Sb_aAl_bS_c$		
		Sb a	Al b	S c
Sb_2S_3	Nominal concentration in the precursor	40	-	60
	EDS (atomic %, ±4%)	42.6	-	57.4
$Sb_{1.9}Al_{0.1}S_3$	Nominal concentration in the precursor	38	2	60
	EDS (atomic %, ±4%)	33.2	6.2	60.6

Figure S1. Energy dispersive X-ray spectra of (a) Sb_2S_3 and (b) $Sb_{1.9}Al_{0.1}S_3$ anodes obtained from a scanning electron microscope.
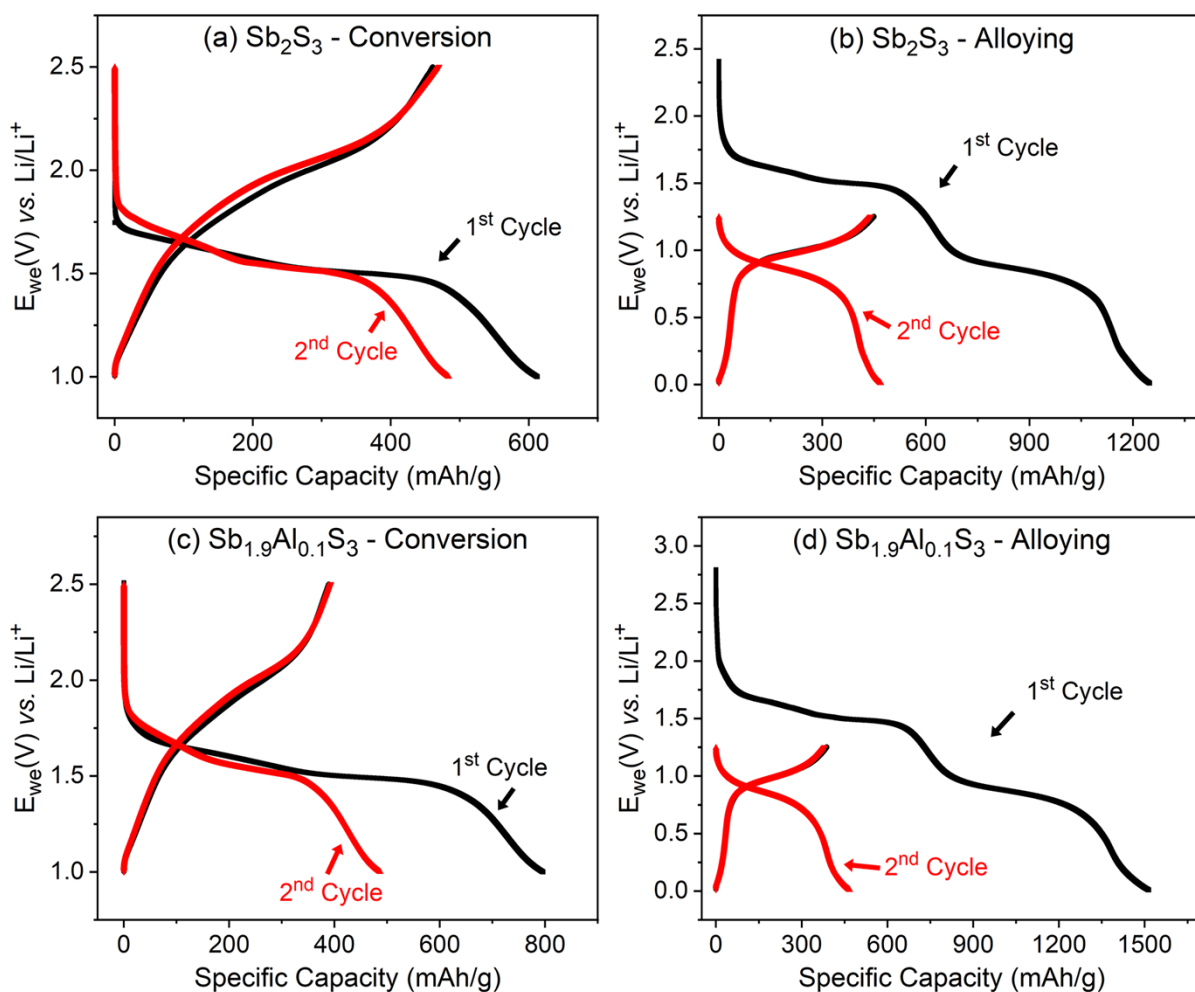
Figure S2. Galvanostatic charge-discharge profiles of Sb_2S_3 when cycled at 0.05C in the (a) conversion regime, i.e., between 2.5 V and 1 V (*vs.* Li/Li$^+$) and (b) alloying regime, i.e., between 1.25 V and 10 mV (*vs.* Li/Li$^+$). Galvanostatic charge-discharge profiles of $Sb_{1.9}Al_{0.1}S_3$ when cycled at 0.05C in the (c) conversion and (d) alloying regimes.
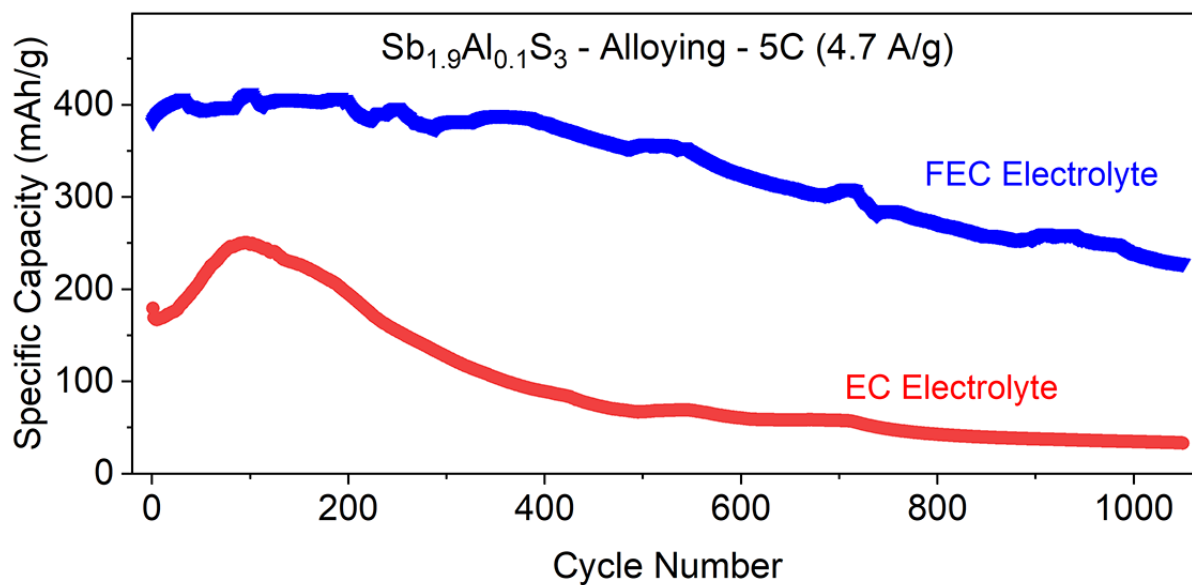
Figure S3. Cycling stability of $Sb_{1.9}Al_{0.1}S_3$-Alloy using FEC and EC electrolytes when cycled at 5C for over 1000 cycles. FEC electrolyte improves the rate capability and cycling stability of the alloy storage in $Sb_{1.9}Al_{0.1}S_3$.
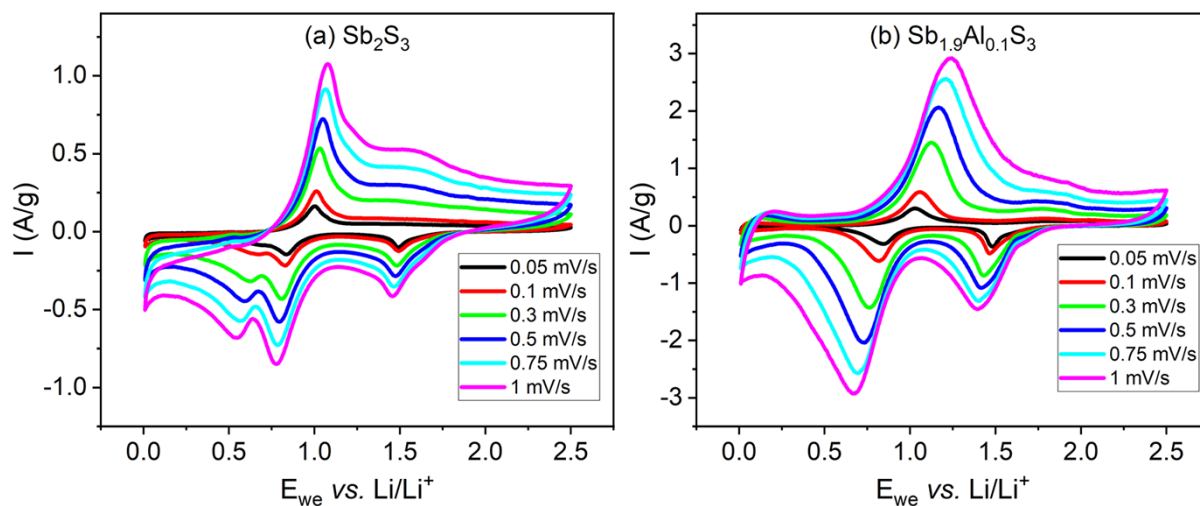
Figure S4. Cyclic voltammetry profiles of (a) Sb_2S_3 and (b) $Sb_{1.9}Al_{0.1}S_3$ when scanned at different rates in both conversion and alloying regimes.

Table S2. Estimated lithium diffusion coefficient in Sb_2S_3 and $Sb_{1.9}Al_{0.1}S_3$ anodes.

Sample	Lithiation (cm^2 s^{-1})	Delithiation (cm^2 s^{-1})
Sb_2S_3	4.7×10^{-11}	7.9×10^{-11}
$Sb_{1.9}Al_{0.1}S_3$	6.6×10^{-10}	6.8×10^{-10}

Cyclic voltammetry was carried out to understand the electrochemical features better, and the observed profiles were plotted in Figure S6. As the scan rate increases, peak separation increases as expected in diffusion-limited systems [1]. The peak current as a function of inverse square root scan rate shows a linear change indicating that the Randle Sevick equation (Equation S1) can be used to estimate the diffusion coefficient [2].

$$\frac{i_p}{m} = 0.4463 \left(\frac{F}{RT}\right)^{1/2} C_{Li} \, \nu^{1/2} \, A_e \, D_{Li}^{1/2}$$

Equation S1.

where i_p/m is the normalized peak current (A g^{-1}), F is the Faraday constant (96485.33 C mol^{-1}), R is the universal gas constant (8.314 J mol^{-1} K^{-1}), C_{Li} is the concentration of Li ions (0.0133 mol cm^{-3}) [3], ν is the scan rate (V s^{-1}), and A_e is the active surface area of the electrode material (1.767 cm^2) and D_{Li} the diffusion coefficient of lithium in the electrode.
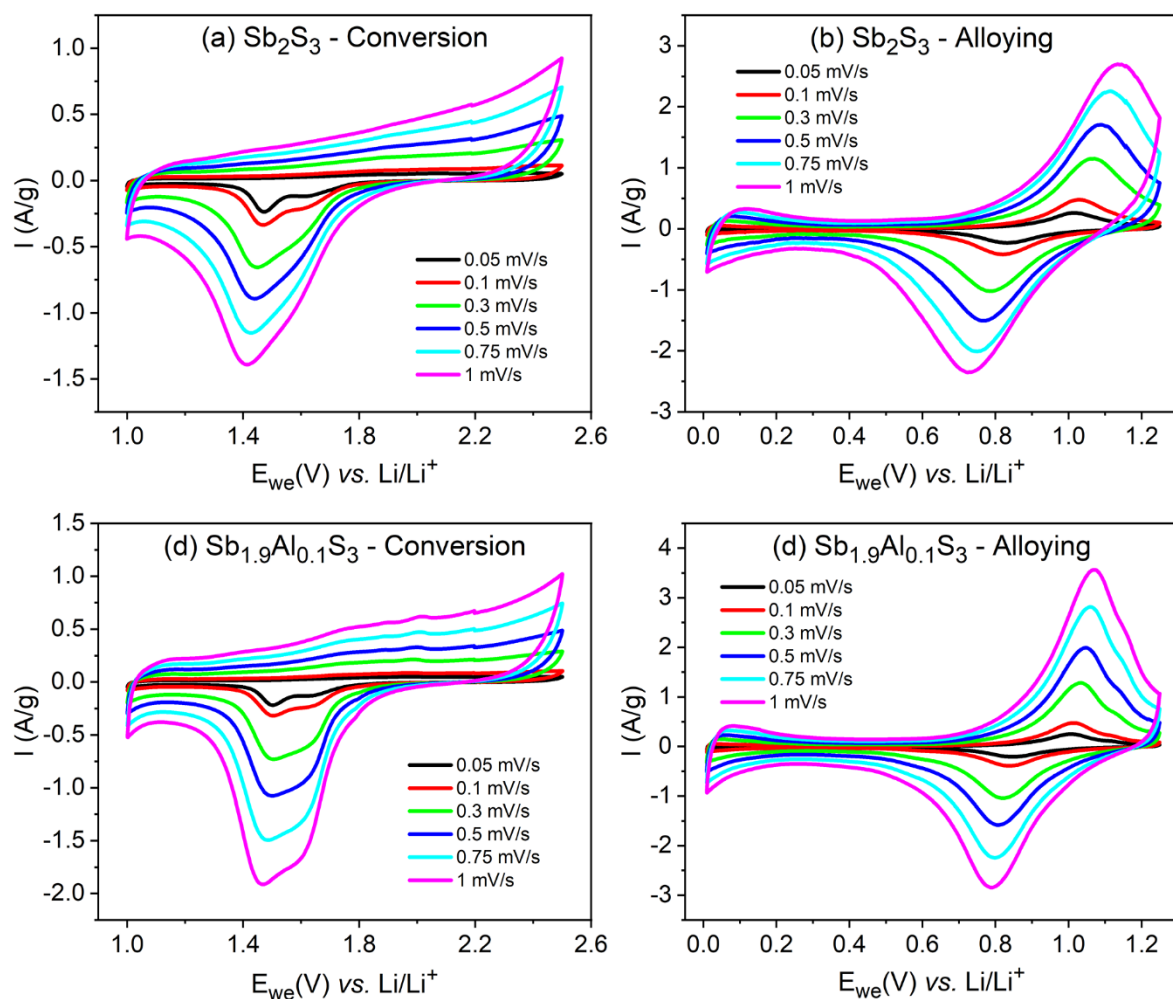
Figure S5. Cyclic voltammetry plots of Sb_2S_3 in (a) Conversion and (b) Alloying regimes, of $Sb_{1.9}Al_{0.1}S_3$ in (c) Conversion and (d) Alloying regimes.

Table S3. The estimated lithium diffusion coefficient in Sb_2S_3 and $Sb_{1.9}Al_{0.1}S_3$ anodes.

	Lithiation (cm^2 s^{-1})	Delithiation (cm^2 s^{-1})
Sb_2S_3-Alloy	4.4×10^{-10}	5.7×10^{-10}
$Sb_{1.9}Al_{0.1}S_3$-Alloy	6.4×10^{-10}	1.0×10^{-9}

In alloying, the peaks are sharper. In the $Sb_{1.9}Al_{0.1}S_3$ anode, no new peaks were observed, and the normalized current is larger, indicating that Al does not change the lithium storage mechanism but improves the performance of the anodes. The diffusion coefficient estimated from the alloy storage of the anodes is shown in Table S3. Peaks in conversion storage are too smeared for estimating the lithium diffusion coefficient.

The lithium diffusion coefficient in $Sb_{1.9}Al_{0.1}S_3$-Alloy is much larger than in other storage regimes, indicating the reason for enhanced electrochemical properties. Also, it should be noted that the delithiation diffusion coefficient is always larger than the lithiation diffusion coefficient, irrespective of the cut-off voltages used. This suggests that the capacity loss is primarily due to lithium not getting into the Sb_2S_3 system. This explains the observation of nanorods in scanning electron micrographs of Sb_2S_3 anode cycled in alloying and conversion regime (Figure 6(b)). These nanorods are the ones which have not participated in the electrochemical lithium storage. In the case of $Sb_{1.9}Al_{0.1}S_3$ cycled in conversion and alloy regime, Figure 6(f), all the nanorods participated in lithium storage, underwent pulverization, and lost the microstructure resulting in the formation of the nanoparticles (Figure 6 (f)).
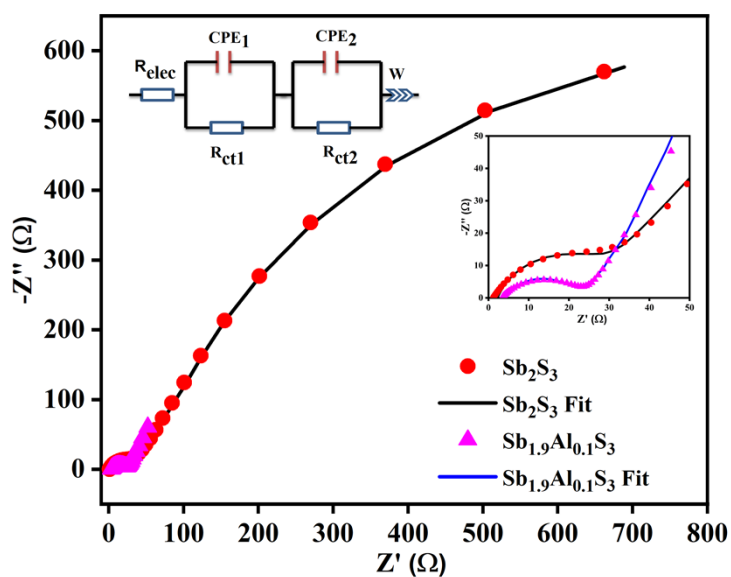
Figure S6. Electrochemical impedance spectroscopy studies on Sb_2S_3 and $Sb_{1.9}Al_{0.1}S_3$ anodes after cycling in the alloying regime. The profile of Sb_2S_3 shows two complete semicircles and one incomplete semicircle. The region dominated by lithium diffusion (Warburg) is yet to be seen. In the $Sb_{1.9}Al_{0.1}S_3$ anode, two semicircles are observed, after which lithium diffusion dominates the system behavior.

EIS studies were carried out after alloying to understand the electrochemical features better, and the observed profiles were plotted in Figure S8. In Sb_2S_3, two broad semicircles are present, followed by an incomplete semicircle. In the $Sb_{1.9}Al_{0.1}S_3$ anode, two semicircles are observed, followed by the Warburg element (see the inset in Figure S8). In Sb_2S_3, the second semicircle starts dominating when the frequency is 122 Hz, whereas, in the case of $Sb_{1.9}Al_{0.1}S_3$, the Warburg element starts dominating at 44 Hz, indicating the better lithium diffusion kinetics in $Sb_{1.9}Al_{0.1}S_3$ anode. The intercept on the x-axis is the electrolyte resistance [4], which is a little larger for the $Sb_{1.9}Al_{0.1}S_3$ anode, probably because of the dissolution of byproducts from the SEI layer formation [5]. The first semicircle attributable to the solid electrolyte interface layer is much larger for Sb_2S_3 than it is for $Sb_{1.9}Al_{0.1}S_3$, indicating a stable SEI layer on the latter. This could be attributed to the smaller volume expansion of $Sb_{1.9}Al_{0.1}S_3$, as observed from post-electrochemical scanning electron microscopy studies in Figure 6. In Sb_2S_3, the second semicircle is extremely large, indicating huge charge transfer resistance. In the $Sb_{1.9}Al_{0.1}S_3$ anode, the charge transfer resistance is much smaller. It is possible that the larger Sb nanoparticles which formed during the decomposition of $Sb_{1.9}Al_{0.1}S_3$ formed a percolation network in Li_2S and other polysulfide matrix, very likely in contact with other particles

decreasing the effective resistance over the length of the electrode film [6]. Sb_2S_3, with amorphous Sb nanoparticles, is not likely to have such a percolation network resulting in huge charge transfer resistance. In Sb_2S_3, the beginning of a third semicircle is observed, but it is not fully observable. Very likely, it is a contribution from the polysulfides left over from the previous conversion reaction [7]. In $Sb_{1.9}Al_{0.1}S_3$, such a third semicircle is not seen. Rather lithium diffusion starts to dominate the system behavior as seen from the linear profile (Warburg element). The estimated fit parameters are shown in Table S4.

Table S4: Estimated parameters from the EIS fitting.

	Sb_2S_3	$Sb_{1.9}Al_{0.1}S_3$
R_{elec} (Ω)	1	3
R_{ct1} (Ω)	23	20
R_{ct2} (Ω)	740	1050

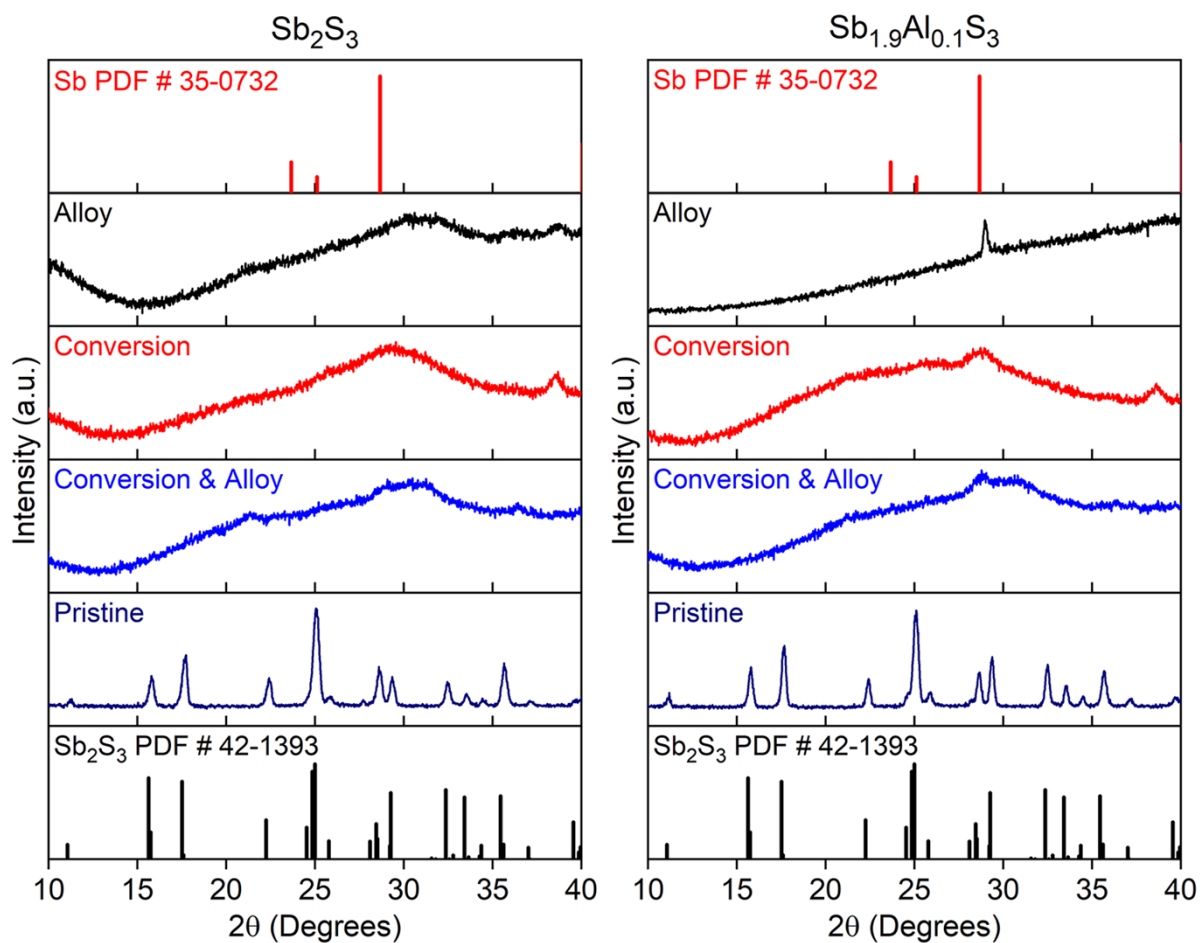**Figure S7.** Powder X-ray diffraction patterns of Sb_2S_3 and $Sb_{1.9}Al_{0.1}S_3$ cycled in alloying, conversion and both regimes. Powder X-ray diffraction patterns of the pristine foil are also shown. Standard powder diffraction patterns of Sb_2S_3 (PDF # 42-1393) and Sb metal (PDF # 35-0732) are shown.
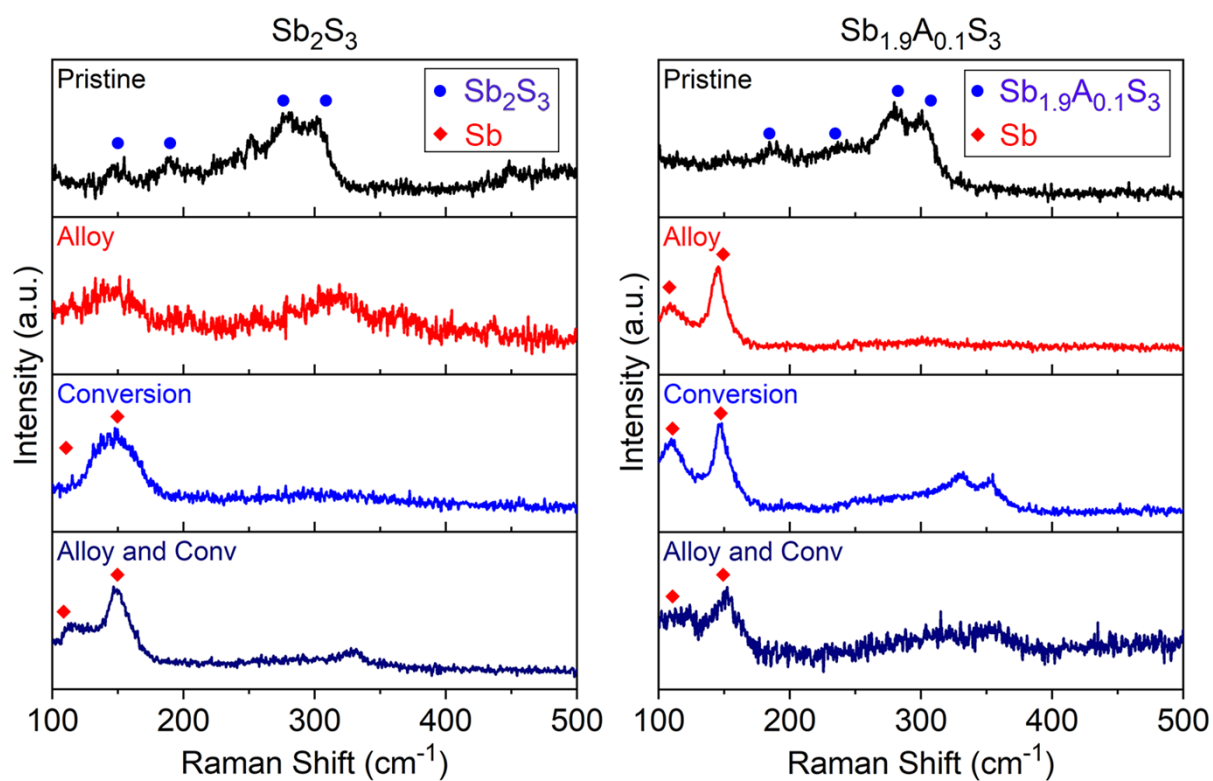
Figure S8. Post electrochemical Raman spectral studies on pristine and cycled Sb_2S_3 and $Sb_{1.9}Al_{0.1}S_3$ anodes (in the lithiated state) after cycling in different regimes. Circles represent peaks attributable to stibnite structure. Diamonds represent peaks attributable to metallic Sb. The peaks of metallic Sb are much sharper in the $Sb_{1.9}Al_{0.1}S_3$-Alloy anode, suggesting a larger crystallite size [8].

Table S5. Performance of pristine Sb_2S_3 of different morphology reported in the literature in comparison to this work. All the data correspond to both conversion and alloying regimes (2.5 V to 10 mV *vs* Li/Li$^+$) unless mentioned otherwise.

Morphology	Particle size	Reversible capacity # of cycles at current rate	Capacity (E) at max current rate tested (F)	Reference
Amorphous Sb_2S_3	Film of thickness 950 nm on SS substrate	585.4 mAh/g 250 ~0.2 A/g	467.1 mAh/g (1 A/g)	[9]
Bulk Sb_2S_3	10-20 μm	800 mAh/g 50 0.25 A/g	580 mAh/g (2 A/g)	[10]
Colloidal Sb_2S_3	20-25 nm	400 mAh/g* 1200 2.4 A/g	608 mAh/g (12 A/g)	[4]
Sb_2S_3 nanorod-bundles	dia ~ 100 nm	614 mAh/g 30 0.1 A/g	400 mAh/g (0.5 A/g)	[11]
Sb_2S_3 Hollow Microspheres	2-3 μm	674 mAh/g 50 0.2 A/g	541 mAh/g (5 A/g)	[12]
Ultrathin Sb_2S_3 nanosheets	thickness ~ 3.8 nm	800 mAh/g 200 0.2 A/g	607 mAh/g (2 A/g)	[13]
Sb_2S_3 nanorods – conversion and alloying	dia ~ 200 nm length ~10 μm	31.7 mAh/g 500 4.7 A/g	37.4 mAh/g (18.8 A/g)	**This work**
$Sb_{1.9}Al_{0.1}S_3$ nanorods – conversion and alloying	dia ~ 200 nm length ~10 μm	71.4 mAh/g 500 4.7 A/g	292.1 mAh/g (18.8 A/g)	**This work**
$Sb_{1.9}Al_{0.1}S_3$ nanorods – conversion	dia ~ 200 nm length ~10 μm	23 mAh/g 1000 4.7 A/g [#]	32.6 mAh/g (37.6 A/g)	**This work**
$Sb_{1.9}Al_{0.1}S_3$ nanorods - alloying	**dia ~ 200 nm length ~10 μm**	**239.8 mAh/g 1000 4.7 A/g [#]**	**49.3 mAh/g (37.6 A/g)**	**This work**

* Estimated from the published graph. # Measurements were carried out on a different set of coin cells.

Note: 1C = 0.946 A/g

Table S6. Performance of different materials tested as anodes for lithium-ion batteries reported in the literature.

Anode	Theoretical capacity (mAh/g)	Voltage *vs.* Li/Li$^+$ (V)	Reversible capacity (A) after (B) cycles at current rate (C)	Capacity (E) at max current rate tested (F)	Reference
Graphite	372	~0.3	~70 (50) 1C	~25 (2C)	[14]
$Li_4Ti_5O_{12}$	170	~1.5	157 (50) 1C	96 (20C)	[15]
MoS_2	670	~1.7	1043 (100) 0.15C	680 (1.5C)	[16]
Rutile TiO_2	170	~1.5	160.4 (100) 1C	105.6 (10C)	[17]
Graphene	372-1116	~1	460 (100) 1C	650 (1C)	[18]
Silicon	4200	~0.5	1801 (40) 0.2C	~1000 (2C)	[19]
Multi-wall CNT	372-1116	~1.5	~900 (50) 1C	767 (3C)	[20]
Lithium	3860	0	-	-	[21]
Sb_2S_3	946	~1	614 (30) 0.1C[#]	400 (0.5C)[#]	[11]
$Sb_{1.9}Al_{0.1}S_3$ – Only Alloying	**473**	**~0.7**	**450 (5) 0.1C*** **239.8 (1000) 5C**	**231.6 (10C)*** **49.3 (40C)**	**This work**

*Measurement on different cells

Approximate C-rates

References:

[1]   M. Weiss, R. Ruess, J. Kasnatscheew, Y. Levartovsky, N.R. Levy, P. Minnmann, L. Stolz, T. Waldmann, M. Wohlfahrt-Mehrens, D. Aurbach, M. Winter, Y. Ein-Eli, J. Janek, Fast Charging of Lithium-Ion Batteries: A Review of Materials Aspects, Adv. Energy Mater. 11 (2021) 2101126. https://doi.org/10.1002/aenm.202101126.

[2]   A.J. Bard, L.R. Faulkner, H.S. White, Electrochemical methods: fundamentals and applications, John Wiley & Sons, 2022.

[3]   J. Xie, J. Xia, Y. Yuan, L. Liu, Y. Zhang, S. Nie, H. Yan, X. Wang, Sb_2S_3 embedded in carbon–silicon oxide nanofibers as high-performance anode materials for lithium-ion and sodium-ion batteries, J. Power Sources. 435 (2019) 226762. https://doi.org/10.1016/j.jpowsour.2019.226762.

[4]   K. V. Kravchyk, M. V. Kovalenko, M.I. Bodnarchuk, Colloidal Antimony Sulfide Nanoparticles as a High-Performance Anode Material for Li-ion and Na-ion Batteries, Sci. Rep. 10 (2020) 2554. https://doi.org/10.1038/s41598-020-59512-3.

[5]   R. Jung, M. Metzger, D. Haering, S. Solchenbach, C. Marino, N. Tsiouvaras, C. Stinner, H.A. Gasteiger, Consumption of Fluoroethylene Carbonate (FEC) on Si-C Composite Electrodes for Li-Ion Batteries, J. Electrochem. Soc. 163 (2016) A1705–A1716. https://doi.org/10.1149/2.0951608jes.

[6]   A.K. Budumuru, B. Rakesh, C. Sudakar, Enhanced high rate capability of Li intercalation in planar and edge defect-rich MoS_2 nanosheets, Nanoscale. 11 (2019) 8882–8897. https://doi.org/10.1039/c9nr02043h.

[7]   M. Wild, L. O'Neill, T. Zhang, R. Purkayastha, G. Minton, M. Marinescu, G.J. Offer, Lithium sulfur batteries, a mechanistic review, Energy Environ. Sci. 8 (2015) 3477–3494. https://doi.org/10.1039/C5EE01388G.

[8]   N.E. Drewett, I.M. Aldous, J. Zou, L.J. Hardwick, In situ Raman spectroscopic analysis of the lithiation and sodiation of antimony microparticles, Electrochim. Acta. 247 (2017) 296–305. https://doi.org/10.1016/j.electacta.2017.07.030.

[9]   Q. Wang, Y. Lai, F. Liu, L. Jiang, M. Jia, Amorphous Sb_2S_3 Anodes by Reactive Radio Frequency Magnetron Sputtering for High-Performance Lithium-Ion Half/Full Cells, Energy Technol. 7 (2019) 1900928. https://doi.org/10.1002/ente.201900928.

[10] D.Y.W. Yu, H.E. Hoster, S.K. Batabyal, Bulk antimony sulfide with excellent cycle stability as next-generation anode for lithium-ion batteries, Sci. Rep. 4 (2014) 4562. https://doi.org/10.1038/srep04562.

[11] X. Zhou, S. Hua, L. Bai, D. Yu, Synthesis and electrochemical performance of hierarchical Sb_2S_3 nanorod-bundles for lithium-ion batteries, J. Electrochem. Sci. Eng. 4 (2014) 45–53. https://doi.org/10.5599/jese.2014.0045.

[12] J. Xie, L. Liu, J. Xia, Y. Zhang, M. Li, Y. Ouyang, S. Nie, X. Wang, Template-Free Synthesis of Sb_2S_3 Hollow Microspheres as Anode Materials for Lithium-Ion and Sodium-Ion Batteries, Nano-Micro Lett. 10 (2017) 12. https://doi.org/10.1007/s40820-017-0165-1.

[13] S. Yao, J. Cui, Y. Deng, W.G. Chong, J. Wu, M. Ihsan-Ul-Haq, Y.W. Mai, J.K. Kim, Ultrathin Sb_2S_3 nanosheet anodes for exceptional pseudocapacitive contribution to multi-battery charge storage, Energy Storage Mater. 20 (2019) 36–45. https://doi.org/10.1016/j.ensm.2018.11.005.

[14] J. Billaud, F. Bouville, T. Magrini, C. Villevieille, A.R. Studart, Magnetically aligned graphite electrodes for high-rate performance Li-ion batteries, Nat. Energy. 1 (2016) 16097. https://doi.org/10.1038/nenergy.2016.97.

[15] W. Zhang, J. Li, Y. Guan, Y. Jin, W. Zhu, X. Guo, X. Qiu, Nano-$Li_4Ti_5O_{12}$ with high rate performance synthesized by a glycerol assisted hydrothermal method, J. Power Sources. 243 (2013) 661–667. https://doi.org/10.1016/j.jpowsour.2013.06.010.

[16] X. Zuo, K. Chang, J. Zhao, Z. Xie, H. Tang, B. Li, Z. Chang, Bubble-template-assisted synthesis of hollow fullerene-like MoS_2 nanocages as a lithium ion battery anode material, J. Mater. Chem. A. 4 (2015) 51–58. https://doi.org/10.1039/c5ta06869j.

[17] T. Lan, Y. Liu, J. Dou, Z. Hong, M. Wei, Hierarchically porous TiO_2 microspheres as a high performance anode for lithium-ion batteries, J. Mater. Chem. A. 2 (2014) 1102–1106. https://doi.org/10.1039/c3ta14178k.

[18] G. Wang, X. Shen, J. Yao, J. Park, Graphene nanosheets for enhanced lithium storage in lithium ion batteries, Carbon N. Y. 47 (2009) 2049–2053. https://doi.org/10.1016/j.carbon.2009.03.053.

[19] J. Wan, A.F. Kaplan, J. Zheng, X. Han, Y. Chen, N.J. Weadock, N. Faenza, S. Lacey, T.

Li, J. Guo, L. Hu, Two dimensional silicon nanowalls for lithium ion batteries, J. Mater. Chem. A. 2 (2014) 6051–6057. https://doi.org/10.1039/c3ta13546b.

[20]   I. Lahiri, S.W. Oh, J.Y. Hwang, S. Cho, Y.K. Sun, R. Banerjee, W. Choi, High capacity and excellent stability of lithium ion battery anode using interface-controlled binder-free multiwall carbon nanotubes grown on copper, ACS Nano. 4 (2010) 3440–3446. https://doi.org/10.1021/nn100400r.

[21]   D. Lin, Y. Liu, Y. Cui, Reviving the lithium metal anode for high-energy batteries, Nat. Nanotechnol. 12 (2017) 194–206. https://doi.org/10.1038/nnano.2017.16.